

# Thermal and Optical Properties of $Zn_{1-x}Mn_xTe$ Diluted Magnetic Semiconductor Studied by Photoacoustic Spectroscopic Method

B. K. Sarkar · A. S. Verma · R. C. Gupta ·  
K. Singh

Received: 16 June 2009 / Accepted: 13 May 2010 / Published online: 1 June 2010  
© Springer Science+Business Media, LLC 2010

**Abstract** Using photoacoustic spectroscopy, the composition-dependent absorption coefficient ( $\alpha$ ), thermal diffusivity ( $\sigma$ ), and optical bandgap ( $E_g$ ) of  $Zn_{1-x}Mn_xTe$  diluted magnetic semiconductor have been measured. For higher Mn compositions, the absorption spectrum of the Zn–Mn–Te system consists of three regions, viz., the high absorption region, the exponential region, and the weak absorption tail. The bandgap follows a nonlinear variation with composition, showing a downward bowing with a minimum around  $x = 0.31$  as a consequence of the electro-negativity difference between the substituted atoms. The composition-dependent band-edge effective mass of the carriers does not show the bowing behavior indicating that the momentum matrix is not the same for all the  $Zn_{1-x}Mn_xTe$  alloys due to different lattice constants. The absorption spectra show that the transition is allowed and direct.

**Keywords** Absorption coefficient · Diluted magnetic semiconductor · Optical bandgap · Photoacoustic spectroscopy · Thermal diffusivity

---

B. K. Sarkar (✉)

Department of Physics (SAS), VIT University, Technology Tower, Room 411, Vellore,  
632014 TN, India

e-mail: bks@physics.org.in

A. S. Verma

Department of Physics, Panjab University, Chandigarh 160014, India

R. C. Gupta · K. Singh

Department of Physics, B.S.A. College, Mathura 281001, India

## 1 Introduction

Diluted magnetic semiconductors (DMSs) have long been of great interest due to the combination of two large branches in materials science, semiconductors and magnetism. They are “diluted magnetic” semiconductors in a sense that these semiconducting alloys have a lattice made up in part of substitutional magnetic atoms. A great deal of attention has been attributed to the study of diluted magnetic semiconducting alloys from the technological point of view that they can add a new degree of freedom associated with the spin of carriers to the electronic as well as optical semiconductor devices. The most extensive and thorough study of DMSs has been concentrated mostly on  $A_{1-x}^{II}Mn_xB^{VI}$  alloys [1] in which a fraction of the group II sub-lattice is replaced by Mn which is attributed to the random distribution of magnetic ions over the cation sublattice with the formation of the spin-glass-like phase [2,3]. The presence of localized magnetic ions in these semiconductor alloys leads to an exchange interaction between the sp band electrons and the d electrons associated with  $Mn^{++}$ , resulting in large Zeeman splittings of electronic (band and impurity) levels. This selective enhancement of spin-dependent properties gives rise to antiferromagnetic cluster formation [4] and magnon excitations [5]. Due to the presence of magnetic ions in the lattice, the spin–spin exchange interaction between the localized magnetic moments and the band electrons [6] affects the energy band and impurity level parameters of these materials (e.g., by exchanging electronic g-factors). The substitutional Mn atoms in the  $A^{II}B^{VI}$  lattice are also characterized by highly efficient electroluminescence, which makes dilute  $A_{1-x}^{II}Mn_xB^{VI}$  alloys in the context of optical flat panel display applications. Such novel and potentially important phenomena as the magnetic field-induced overlap between valence and conduction bands occurring in  $Hg_{1-x}Mn_xTe$  and  $Hg_{1-x}Mn_xSe$  [7], extremely large Faraday rotation in  $Cd_{1-x}Mn_xTe$  [8], giant magnetoresistance associated with hopping conduction in  $Hg_{1-x}Mn_xTe$  [9], and the magnetic polaron observed in  $Cd_{1-x}Mn_xSe$  [10,11] are all consequences of the spin–spin exchange interaction. The tunability of the lattice parameters and the energy gaps of the  $A_{1-x}^{II}Mn_xB^{VI}$  alloys make them excellent candidates for the preparation of quantum wells, superlattices, and for bandgap technology applications. The presence of Mn in these alloys gives new shape to the magnetic properties, optical transitions specific to  $Mn^{++}$  ions, and the sp–d exchange interaction into the multiple quantum-well field.

A great deal of work has been devoted to the investigation of optical properties of II–VI compounds and their ternary alloys [12,13]. The energy bandgap of these semiconductors has a value between 1 eV and 3 eV [14–16] which makes them useful for applications in optoelectronic devices in the visible region of the spectrum. But very little investigation of the thermal properties of II–VI compounds has been reported [17]. In this paper we have investigated the thermal diffusivity, optical absorption, and energy bandgap near the fundamental edge of  $Zn_{1-x}Mn_xTe$  ( $0 \leq x \leq 1$ ) type polycrystalline alloys in the visible spectral region using a high resolution photoacoustic spectrometer (PAS) [18,19]. The nonradiative absorption processes which are associated with the band structure, defect-related energy loss mechanisms, etc., can be directly and very accurately obtained from analysis of photoacoustic spectroscopic (PAS) spectra [20,21].

## 2 Experimental

For preparation of the samples,  $\text{Zn}_{1-x}\text{Mn}_x\text{Te}$  ( $x = 0.0, 0.086, 0.17, 0.26$ ),  $\text{ZnTe}$ , and  $\text{MnTe}$  (each of purity 99.99 %) are used as starting materials. The desired amount of the mixture is ground to powder and pressed into thin pellets. These pellets are sealed in an evacuated quartz tube and placed inside the furnace at about 1400 °C to 1450 °C for 2 days. The ampoules were then furnace cooled at room temperature. The samples thus prepared were crystalline in nature, and their composition and structure were tested by X-ray powder diffraction (Phillips:Model PW 1710) studies with  $\text{CuK}\alpha$  having angular distribution of the range  $15^\circ \leq \theta \leq 40^\circ$ . The energy dispersive X-ray (EDX) experiment (Model KEVEV 3600-0388, USA) confirms the ratio of the constituent atoms within  $\pm 2\%$ . The lattice constants are given in Table 1. The constants were verified according to Vegard's law.

The single beam PAS used in the present investigation consists of a PA cell containing a sensitive microphone, a 1000 W Xe lamp with power supply (Muller, type SVX 1000, Germany), monochromator (Oriel 77250), and a mechanical chopper (SR540) discussed elsewhere [18, 22]. In PAS, one has to detect the photoacoustic (PA) signal produced when a sample placed in a cell is irradiated by an intensity modulated beam of light. The amplitude and phase of the PA signal depends on the thermal and optical properties of the sample, the most important of which are the specific heat, thermal conductivity, thermal diffusivity, optical absorption coefficient, etc. Hence, the wealth of information contained in the PA signal can be used to investigate the thermal and optical properties of solids. The PA signal produced is detected by a sensitive microphone (Brüel and Kjaer 4147) and processed by using a preamplifier and lock-in amplifier (SR530). To minimize the light scattering [23, 24], very thin (~3 mm to 4 mm diameter and ~0.3 mm thick) samples were used for the PAS studies. With the thickness of the sample being very small in comparison to the surface, a one-dimensional piston vibration model has been considered to detect the PA signal produced when the sample was placed in the cell. The detail of cell fabrication was discussed in another work of the present author [22]. All the spectra were recorded at room temperature using a chopping frequency of 120 Hz. The optical bandgap is determined by measuring the variation of the normalized PA signal intensity with the wavelength of the incident light. The PA spectrum obtained from highly absorbing carbon black powder was used to normalize the spectrum of the samples.

**Table 1** Characteristic parameters of the  $\text{Zn}_{1-x}\text{Mn}_x\text{Te}$  ( $0 \leq x \leq 1$ ) alloys

Sample	Lattice constant $a$	Transition power factor $n$ (used in Eq. 4)	Thermal diffusivity $\sigma(\text{cm}^2 \cdot \text{s}^{-1})$	$E_g$ (eV)	Effective mass ratio ( $m^*/m$ )
ZnTe	6.101	0.467	0.0216	2.281	0.186
$\text{Zn}_{0.6}\text{Mn}_{0.4}\text{Te}$	6.194	0.503	0.0193	2.238	0.188
$\text{Zn}_{0.2}\text{Mn}_{0.8}\text{Te}$	6.287	0.492	0.0251	2.372	0.198
MnTe	6.334	0.508	0.0256	2.431	0.208

The thermal diffusivity ( $\sigma$ ) and energy gap  $E_g$  are obtained from Figs. 2 and 5, respectively. Effective mass ratio ( $m^*/m$ ) is calculated from Eq. 10

### 3 Results and Discussion

#### 3.1 Absorption Coefficient and Bandgap

The normalized PA spectra of  $Zn_{1-x}Mn_xTe$  ( $0 \leq x \leq 1$ ) as a function of incident wavelength are shown in Fig. 1. The optical absorption coefficient  $\alpha$  for thermally thick samples is calculated from the relation [25, 26],

$$a = \frac{q^2 + q (2 - q^2)^{1/2}}{m (1 - q^2)} \quad (1)$$

where  $q$  is the normalized PA signal intensity.  $\mu$  is the thermal diffusion length given by [20, 21]

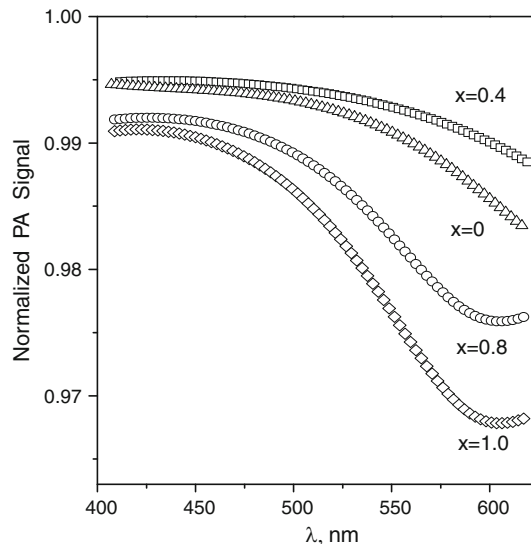
$$\mu = \left( \frac{2\sigma}{\omega} \right)^{1/2} = \left( \frac{f_c l^2}{\pi f} \right)^{1/2} \quad (2)$$

where  $\omega = 2\pi f$  ( $f$  is the modulation chopping frequency and  $f_c$  is the characteristic modulation chopping frequency).  $\sigma$  is the thermal diffusivity, and  $l$  is the sample thickness.  $f_c$  and  $l$  are related to the thermal diffusivity as follows [27, 28]:

$$\sigma = f_c l^2 \quad (3)$$

In view of the variation of the PA signal intensity with the modulation chopping frequency, the samples are called thermally thick when  $f > f_c$  and thermally thin when

**Fig. 1** Normalized photoacoustic (PA) spectra of  $Zn_{1-x}Mn_xTe$  system with  $x = 0.0, 0.4, 0.8$ , and  $1.0$  as a function of wavelength of incident light



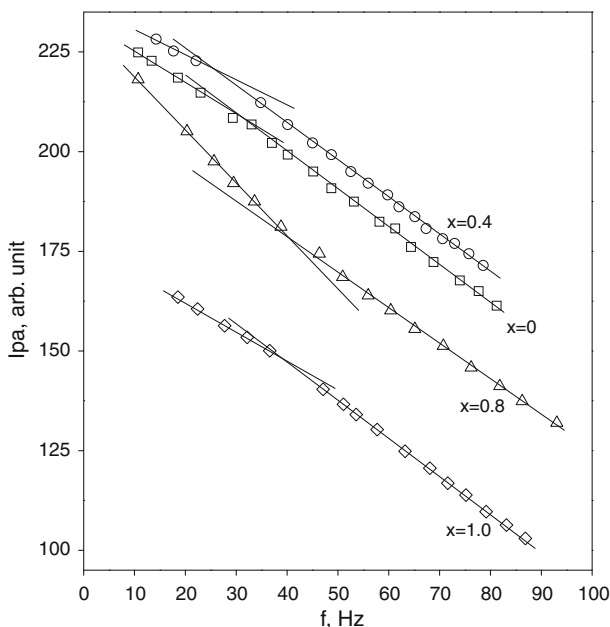
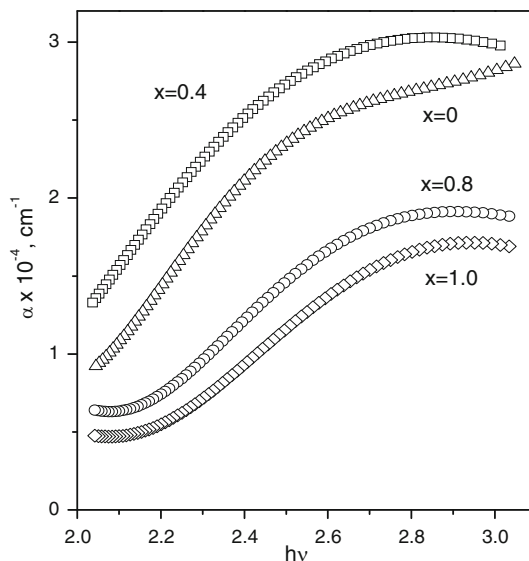


**Fig. 2** PA signal amplitude ( $I_{pa}$ ) versus chopping frequency ( $f$ ) for different values of  $x$  in  $Zn_{1-x}Mn_xTe$ . Characteristic chopping frequency ( $f_c$ ) is determined from the distinct change in slope.  $f_c$  has the values of 24 Hz, 31 Hz, 40 Hz, and 38 Hz for  $x = 0.0, 0.4, 0.8$ , and 1.0

$f < f_c$  ( $f_c$  is the characteristic frequency [27–29] at which the sample transforms from a thermally thin regime to a thermally thick regime). For an appropriate thickness of the sample, one can obtain a cross-over from the thermally thin regime to the thermally thick regime at the characteristic chopping frequency,  $f_c$ . The signal intensity versus chopping frequency shows a change in slope at the characteristic frequency  $f_c$ . Figure 2 shows such a plot of the PA signal amplitude versus the chopping frequency for different Mn compositions in  $Zn_{1-x}Mn_xTe$ . From these curves the characteristic frequencies  $f_c$  (at which frequency a change of slope occurs) were determined for different Mn doping. Using Eq. 3 the thermal diffusivity ( $\sigma$ ) was calculated taking the thickness of the sample pellet as  $\sim 0.3$  mm. The thermal diffusivity of  $Zn_{1-x}Mn_xTe$  is calculated using Eq. 3 as a function of concentration  $x$  and is found to vary nonlinearly with concentration (Table 1). Due to the unavailability of other experimental data of thermal diffusivity  $\sigma$  for the Zn–Mn–Te system, we cannot compare our results with others. These values of  $\sigma$  are, however, comparable with those of As–Se–Te ( $\sigma \sim 2 \times 10^{-2} \text{ cm}^2 \cdot \text{s}^{-1}$ , Ref. [29]) and  $Ge_xTe_{1-x}$  ( $\sigma \sim 2 \times 10^{-2} \text{ cm}^2 \cdot \text{s}^{-1}$ , Ref. [30]) systems.

The variation of the absorption coefficient  $\alpha$  for different samples as a function of the incident photon energy is shown in Fig. 3. The absorption spectrum of the Zn–Mn–Te system consists of three regions, viz., the high absorption region, the exponential region, and the weak absorption tail. These three regions are distinct for higher Mn compositions.

**Fig. 3** Variation of absorption coefficient ( $\alpha$ ) of  $Zn_{1-x}Mn_xTe$  as a function of incident photon energy with  $x = 0.0, 0.4, 0.8$ , and  $1.0$ . Absorption coefficient is determined using Fig. 1 and Eq. 1



The type of transitions was determined by considering the relation between the absorption coefficient ( $\alpha$ ) and the photon energy ( $h\nu$ ). They are related as

$$\alpha h\nu = A (h\nu - E_g)^n \quad (4)$$

where  $A$  is a constant and  $n$  is the transition power factor having values of 0.5, 2, 1.5, and 3 for allowed direct, allowed indirect, forbidden direct, and forbidden indirect transitions, respectively [31]. A plot of the logarithm  $\alpha h\nu$  versus  $h\nu$  (Fig. 4) determines the values of  $n$  for different Mn compositions as shown in Table 1. For all

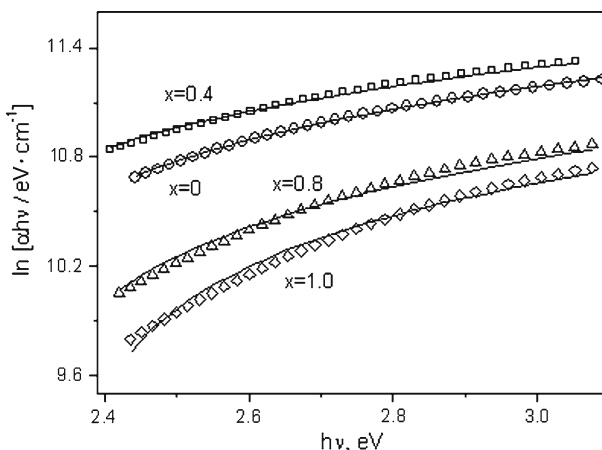


**Fig. 4** Plot of  $\ln(\alpha h\nu)$  versus  $h\nu$  for  $Zn_{1-x}Mn_xTe$ . Solid lines represent theoretical curve fits taking relation as  $\ln(\alpha h\nu) = B + n \ln(h\nu - E_g)$  using Eq. 4. Values of  $n$  for different Mn compositions are given in Table 1

samples, the value of  $n$  is approximately 0.5 which describes the transition as direct in nature in the higher photon energy region. For an allowed and direct transition in the high absorption region [19, 20],

$$\alpha h\nu = A (h\nu - E_g)^{0.5} \quad (5)$$

and after rearrangement, it can be written as

$$(\alpha h\nu)^2 = B (h\nu - E_g) \quad (6)$$

The direct transition in this system is confirmed from the plot of  $(\alpha h\nu)^2$  versus  $h\nu$  for various compositions as shown in Fig. 5. The values of the corresponding optical bandgap ( $E_g$ ) are estimated (where the extrapolated dotted lines meet the abscissa). It is found that the variation of  $E_g$  with composition ( $x$ ) is nonlinear in nature (Fig. 6) obeying the relation  $E_g(x) = 2.276 - 0.209x + 0.376x^2$ . In the variation of the optical bandgap, a distinct downward bowing with a minimum corresponding to the value of  $x$  around 0.31 is observed. A similar kind of optical bowing was reported in the Zn–Se–Te system by Ebina et al. [32] from reflectivity measurements. The dependence of the bandgap on composition is often described by the relation [33],

$$E_g(x) = E_g(\text{ZnTe}) + [E_g(\text{MnTe}) - E_g(\text{ZnTe}) - b]x + bx^2 \quad (7)$$

where  $E_g(\text{ZnTe})$  and  $E_g(\text{MnTe})$  are values of the energy gap for  $x = 0$  and 1, respectively, and  $b = 0.3904 \text{ eV}$  is the bowing parameter. A curve fit according to Eq. 7 has been attempted to our experimental data (shown as a solid curve in Fig. 6). It appears from Fig. 6 that for Zn-rich compositions ( $x \ll 1$ ),  $E_g$  varies slowly with  $x$  whereas it varies faster at the MnTe end of the compositional variation of  $E_g$ . The

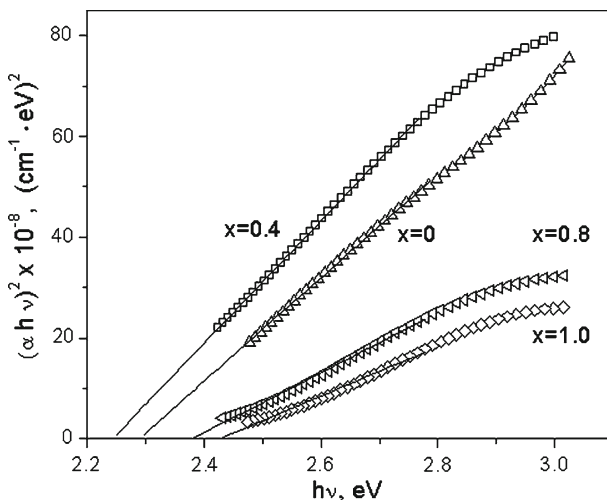
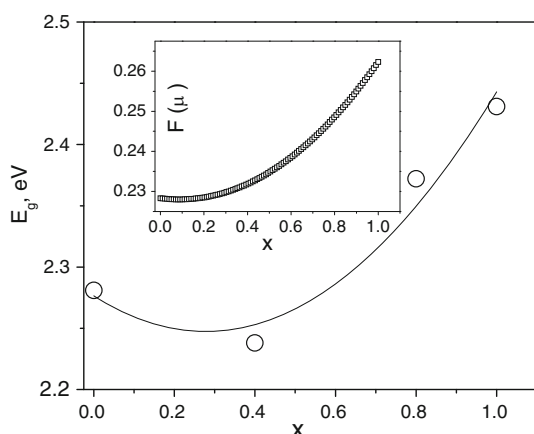


**Fig. 5** Plot of  $(\alpha h\nu)^2$  versus  $h\nu$  for  $\text{Zn}_{1-x}\text{Mn}_x\text{Te}$  with  $x = 0.0, 0.4, 0.8$ , and 1.0

**Fig. 6** Variation of bandgap ( $E_g$ ) with composition ( $x$ ), estimated from Fig. 5 indicating an optical downward bowing. Solid line represents the best fit to the experimental data of  $Zn_{1-x}Mn_xTe$  with Eq. 7. Inset indicates the variation of  $F(\mu)$  with  $x$  for  $Zn_{1-x}Mn_xTe$  constructed using Eq. 10



electro-negativity difference between the substituting atoms [34] is attributed to the downward bowing in the nonlinear variation of  $E_g$  with composition  $x$ . Due to the electro-negativity difference, there is exchange between the Mn spins and the hole spins. This exchange is proportional to the probability of finding the charge carrier at the Mn site, which in turn can be ascribed to the repulsive interactions between the Mn d levels and the  $\Gamma$ -point valence band states. A mismatch between the Zn–Te and Mn–Te bond lengths deviating from those of the respective binary compounds will cause the p–d exchange interaction between the Mn d levels and the  $\Gamma$ -band states. Based on this exchange phenomena, a small dip in energy gap variation will appear around  $x = 0.4$ . Such a type of composition-dependent variation of  $E_g$  was also observed from diffuse reflectance studies by Larach et al. [35] with Zn–Se–Te alloy powders. As the end member of the  $Zn_{1-x}Mn_xTe$  system, the bandgap values of ZnTe ( $x = 0$ ) and MnTe ( $x = 1$ ) were determined as 2.281 eV and 2.431 eV, respectively (Table 1). The bandgaps of ZnTe and MnTe were reported as 2.27 eV [32] and 2.48 eV [36], respectively, in the literature. In a review article [37] on DMSs, a thorough investigation on the composition-dependent bandgap variation for  $Cd_{1-x}Mn_xTe$  with a virtual crystal approximation (VCA) has been reported. In this article the values of  $E_g$  of MnTe (i.e.,  $x = 1$ ) were determined as 2.85 eV and 3.18 eV at 300 K and 4.2 K, respectively. But the downward bowing in the nonlinear variation is not consistent with such a VCA method.

### 3.2 Band-Edge Effective Mass

We have also calculated the band-edge effective mass ( $m^*$ ) of the carriers for the Zn–Mn–Te system from PAS data using the expression [38],

$$\frac{1}{\mu} = \frac{m}{m^*} = 1 + \frac{p^2}{2mE_0}$$

$$E_0 = \frac{p^2}{2m} \left( \frac{\mu}{1 - \mu} \right) \quad (8)$$

$$= \frac{p^2}{2m} F(\mu) \quad (9)$$

where  $m$  is the free-electron mass,  $p$  is the momentum matrix expressed as  $\hbar R$ , with  $R$  as the smallest reciprocal lattice vector. Reasonably, we can take  $p = \hbar/a$ , where  $a$  is the lattice constant. From Eqs. 9 and 7 we can write

$$\begin{aligned} F(\mu, x) = & K_0(x) F(\mu_{\text{ZnTe}}) + [K_1(x) F(\mu_{\text{MnTe}}) - K_0(x) F(\mu_{\text{ZnTe}}) + K'_0(x)] x \\ & + K'_0(x) x^2 \end{aligned} \quad (10)$$

$$K_0(x) = (a/a_{\text{ZnTe}})^2, \quad K_1(x) = (a/a_{\text{MnTe}})^2, \quad K'_0(x) = \frac{2ma^2b}{\hbar^2}.$$

Assume that Vegard's rule for lattice constants is valid in our case,

$$a(x) = (1-x)a_{\text{ZnTe}} + xa_{\text{MnTe}} \quad (11)$$

$\mu_{\text{ZnTe}}$  and  $\mu_{\text{MnTe}}$  are the effective mass ratios of the material with  $x = 0$  and  $x = 1$ , respectively. The function  $F(\mu, x)$  of the ternary compound Zn–Mn–Te alloys is shown in Fig. 6 (inset) using Eq. 10. The composition-dependent  $F(\mu, x)$  does not show the bowing behavior unlike the composition variation of  $E_g$  since the momentum matrix  $p$  is not constant for all  $\text{Zn}_{1-x}\text{Mn}_x\text{Te}$  alloys due to different lattice constants. The effective mass ratios of two end-member alloys (ZnTe and MnTe) are calculated as 0.186 and 0.206, respectively (Table 1). The same property for ZnTe has been reported as 0.17 in the literature [39].

#### 4 Conclusion

From the PAS studies of the diluted magnetic semiconducting alloys  $\text{Zn}_{1-x}\text{Mn}_x\text{Te}$ , we have determined the Mn composition dependence of the thermal diffusivity, optical absorption coefficient, and bandgap. For higher values of  $x$ , three regions, viz., the high absorption region, the exponential region, and the weak absorption tail, are observed. From the optical absorption spectrum the direct band-to-band transition has been found for the high absorption region. This feature of the PAS data enabled us to determine the values of the bandgap as a function of the Mn composition ( $x$ ). The dependence of  $E_g$  on  $x$  is nonlinear with a downward bowing having a minimum at a particular composition ( $x \sim 0.31$ ), which is attributed to the electro-negativity difference between the substituting atoms,

The present experimental procedure and the theoretical analysis of PAS used for the Zn–Mn–Te system could easily be extended to many other systems such as solar-energy related materials, dilute magnetic semiconductors, and other materials (both crystalline and glassy materials) of current technological interest.

**Acknowledgments** The first author (B. K. S.) would like to express his gratitude to VIT University, Vellore, India for its support and second author (A. S. V) is thankful to University Grant Commission, New Delhi, India, for its support under Dr. D. S. Kothari Post Doctoral Fellowship.

## References

1. J.K. Furdyna, J. Kossut, *Semiconductor and Semimetals*, vol. 25 (Academic Press, New York, 1988)
2. R.R. Galazka, *Lecture Notes on Physics*, vol. 152 (Springer, Berlin, 1982)
3. S.B. Oseroff, Phys. Rev. **25**, 6584 (1982)
4. T. Dolling, T.M. Holden, V.F. Sears, J.K. Furdyna, W. Giriat, J. Appl. Phys. **53**, 7644 (1982)
5. A.K. Ramdas, J. Appl. Phys. **53**, 7649 (1982)
6. J.A. Gaj, J. Phys. Soc. Jpn. **49**, 797 (1980)
7. R.R. Galazka, J. Kossut, *Lecture Notes on Physics*, vol. 32 (Springer, Berlin, 1980)
8. J.A. Gaj, R.R. Galazka, M. Nawrocki, Solid State Commun. **25**, 193 (1978)
9. A. Mycielski, J. Mycielski, J. Phys. Soc. Jpn. **49**, 809 (1980)
10. M. Nawrocki, R. Planel, G. Fishman, R.R. Galazka, Phys. Rev. Lett. **46**, 735 (1981)
11. M. Nawrocki, R. Planel, G. Fishman, R.R. Galazka, Solid State Commun. **48**, 8453 (1983)
12. Y.D. Kim, M.V. Klein, S.F. Ren, Y.C. Chang, H. Luo, N. Samarth, J.K. Furdyna, Phys. Rev. B **49**, 7262 (1994)
13. T. Holden, P. Ram, F.H. Pollak, J.L. Freeouf, B.X. Yang, M.C. Tamargo, Phys. Rev. B **56**, 4037 (1997)
14. S. Lee, F. Michl, U. Rössler, M. Dobrowolska, J.K. Furdyna, Phys. Rev. B **57**, 9695 (1998)
15. H.P. Wagner, M. Kühnelt, W. Langbein, J.M. Hvam, Phys. Rev. B **58**, 10494 (1998)
16. B. Sermage, S. Petiot, C. Tangy, L.S. Dang, R. André, J. Appl. Phys. **83**, 7903 (1998)
17. F. Firszt, S. Legowski, H. Meczynska, J. Szatkowski, J. Zakrzewski, Anal. Sci. **17**, S129 (2001)
18. B.K. Sarkar, S. Chatterjee, R.K. Mukherjee, B.K. Chaudhuri, Mater. Sci. Lett. **16**, 1499 (1997)
19. B.K. Sarkar, B.K. Chaudhuri, Int. J. Thermophys. **26**, 295 (2005)
20. A. Rosencwaig, *Photoacoustics and Photoacoustic Spectroscopy* (Wiley, New York, 1980)
21. Y.H. Pao, *Optoacoustic Spectroscopy and Detection* (Academic Press, New York, 1977)
22. B.K. Sarkar, A.K. Ghosh, G. Banerjee, B.K. Chaudhuri, Ind. J. Pure Appl. Phys. **33**, 253 (1995)
23. A. Mandelis, *Photoacoustic and Thermal Wave Phenomena in Semiconductors* (North-Holland, New York, 1987)
24. A.C. Tam, Rev. Mod. Phys. **58**, 381 (1986)
25. A. Zegadi, M.A. Sifkin, M. Djamin, A.E. Hill, R.D. Tomlinson, Phys. Status Solidi A **133**, 533 (1992)
26. P. Poulet, J. Chambron, R. Unterreiner, J. Appl. Phys. **51**, 1738 (1980)
27. A. Lachaine, P. Poulet, Appl. Phys. Lett. **45**, 953 (1984)
28. P. Charpentier, F. Lepoutre, L. Bertrand, J. Appl. Phys. **53**, 608 (1982)
29. K. Nandakumar, J. Philip, J. Non-Cryst. Solids **144**, 247 (1992)
30. J.C. de Lima, N. Cellia, L.C.M. Miranda, C. Chying An, A.H. Franzan, N.F. Leite, Phys. Rev. B **46**, 14186 (1992)
31. D. Bhattacharya, S. Choudhuri, A.K. Pal, Vacuum **43**, 313 (1992)
32. A. Ebina, M. Yamamoto, T. Takahashi, Phys. Rev. B **6**, 3786 (1972)
33. A.A. Bassam, A.W. Brinkman, G.J. Russell, J. Woods, J. Cryst. Growth **86**, 667 (1998)
34. T. Tinoco, M. Quintero, C. Rincon, Phys. Rev. B **44**, 1613 (1991)
35. S. Larach, R.E. Shrader, D.F. Stocker, Phys. Rev. **108**, 587 (1957)
36. Y.R. Lee, A.K. Ramdas, Solid State Commun. **513**, 861 (1984)
37. J.K. Furdyna, J. Appl. Phys. **64**, R29 (1988)
38. D.K. Ferry, *Semiconductors*, chap. 5 (Macmillan, New York, 1991)
39. B. Roy, *II-IV Compounds*, 1st edn. (Pergamon, Oxford, 1969)